Available online at www.sciencedirect.com
SCIENCE DIRECT®
Journal of Computational Physics 193 (2003) 260–274
JOURNAL OF COMPUTATIONAL PHYSICS
www.elsevier.com/locate/jcp

A 3D incompressible thermal lattice Boltzmann model and its application to simulate natural convection in a cubic cavity

Y. Peng, C. Shu *, Y.T. Chew

Department of Mechanical Engineering, National University of Singapore, 10 Kent Ridge Crescent, Singapore 119260, Singapore

Received 22 April 2003; received in revised form 14 August 2003; accepted 14 August 2003

Abstract

A 3D incompressible thermal lattice Boltzmann model is proposed in this paper to solve 3D incompressible thermal flow problems. Two different particle velocity models of D3Q15 and D3Q19 are incorporated in our thermal model. It is indicated that the present thermal model is simple and easy for implementation. It is validated by its application to simulate the 3D natural convection of air in a cubical enclosure, which is heated differentially at two vertical side walls. Good agreement was obtained between the present results and those from a Navier–Stokes solver.

1. Introduction

Lattice Boltzmann method (LBM) is an ideal mesoscopic approach to solve nonlinear macroscopic conservation equations because of its simplicity and ease for parallelization. For incompressible isothermal flows, the LBM is found to be at least as stable, accurate and computationally efficient, as traditional computational methods [1,2] and has achieved excellent success in different application areas such as multiphase flow and complex fluid phenomena [3]. In contrast, its application at the energy moment level is still struggling with numerical instabilities. A good coverage of the literature review about the thermal LBM is given by Lallemand and Luo [4]. Practically, it is important and sometimes critical to have capability to simulate thermal effects simultaneously with the fluid flow. The temperature distribution in a flow field is of central interest in heat transfer problems. In most geophysical flows, the temperature difference is the driving mechanism for the motion of the fluid. So it is necessary to develop a capable thermal model to simulate the incompressible thermodynamics using LBM.

* Corresponding author. Tel.: +65-6874-6476; fax: +65-6779-1459.
E-mail address: mpeshuc@nus.edu.sg (C. Shu).

0021-9991/$ - see front matter © 2003 Elsevier B.V. All rights reserved.
doi:10.1016/j.jcp.2003.08.008

The earliest work was given by Massaioli et al. [5] using the idea of the passive scalar for the temperature and this scheme is also used for the highly parallel 3D simulations of Rayleigh–Benard turbulence [6].

Currently, there are several attempts to construct the thermal models. Luo [7] suggested that the difficulty of solving thermal problems could be overcome by going back to the Boltzmann equation for dense gases, the time-honored Enskog equation. Its practical value remains to be demonstrated because so far no simulation result has been available.

Alexander et al. [8] proposed the multi-speed scheme that expands the equilibrium function to the third-order of the velocity. But the Prandtl number is fixed at the value of 1/2. This limitation has been partially removed by Chen [9] using a two-time relaxation operator. He also proposed higher-order parametric equilibrium functions [10] to satisfy the full set of thermo-hydrodynamic constraints. Nevertheless, the multi-speed scheme suffers from severe numerical instability and the temperature variation is limited to a narrow range. Chen [11] pointed out that the origin of reducing stability condition is related to the lack of a global H-theorem. Based on this, they stabilized the scheme [12] by identifying a temperature-dependent factor in the equilibrium function that leads directly to the removal of the Galilean invariance artifact, and relaxes the requirement of instantaneous accuracy of this factor. This results in a stable scheme but introduces artificial thermal diffusion, which is strongly dependent on the bulk velocity.

The passive-scalar approach utilizes the fact that the macroscopic temperature satisfies the same evolution equation as a passive scalar if the viscous heat dissipation and compression work done by the pressure are negligible. In the passive-scalar LBM thermal model, the temperature is simulated using a separate distribution function that is independent of the density distribution. So it enhances the numerical stability. Extensive studies of 2D and 3D Rayleigh–Benard convections using this method were made by Shan [13].

The two-distribution functions model, which is called internal energy density distribution function (IEDDF) thermal model by He et al. [14], shows great improvement in the stability over the previous LBM thermal models, although a new set of distribution functions is used to describe the temperature dynamics. It is based on the recent discovery that the lattice Boltzmann isothermal models can actually be derived directly by discretizing the continuous Boltzmann equation in temporal, spatial, and velocity spaces. Following the same procedure, the IEDDF thermal model is derived by discretizing the continuous evolution equation for the internal energy distribution. The model has been successfully used to solve some thermal problems in two dimensions [15,16]. On the other hand, we have to indicate that since the pressure comes from the second moment of the density distribution, and is independent of the internal energy distribution, the method actually solves the passive advection problem.

Attempts are also taken from a different way by using higher isotropy of lattice. Pavol et al. [17] proposed the non-space filling lattices, typically octagons, which offer a higher degree of isotropy, to solve the thermal problems. They have proposed the octagonal lattices in 2D and 3D. Some preliminary simulations for 2D jet flow between plane boundaries held at constant temperatures were reported.

On the other hand, we have to indicate that most applications of the above thermal models are limited to the 2D cases. Though the Rayleigh–Benard convection in 3D has been successfully simulated by Shan [13] using passive-scalar method to a certain degree, only the periodic and Dirichlet boundary conditions are considered. For the engineering thermal applications, they usually contain the solid boundaries and Neumann boundary conditions are often in the presence of the flow configurations. In order to solve the 3D thermal problems for the engineering application, a 3D thermal model based on IEDDF thermal model is proposed in this paper. It uses two distribution functions to model the flow and thermal fields. The density distribution function $f_\alpha(x, e, t)$ is used to simulate the macroscopic density and velocity fields, and the energy density distribution function $g_\alpha(x, e, t)$ is used to simulate the macroscopic temperature field.

The particle velocity models used in our thermal LBM are D3Q15 and D3Q19. In the literature, there are some other particle velocity models for the thermal problem. For example, Qian [18] presented D3Q21 and D3Q25 in his new lattice BGK models, in which a proper internal energy is introduced. Chen [10] proposed D3Q40 for the thermal problem using no nonlinear deviation multi-speed models. Vahala et. al. [19] proposed D3Q41 and D3Q53 for the thermal applications using higher order symmetric and no space filling velocity lattice model. Most of these models have not been applied to the thermal problem. Our D3Q15 and D3Q19 models are simpler than these models. There is no additional particle velocity as compared with the isothermal particle velocity models.

Natural convection flow analysis in 3D enclosures has many thermal engineering applications, such as cooling of electronic devices, energy storage systems and compartment fires. In the present paper, the numerical study of the 3D natural convection in an air-filled cubical enclosure, which is heated differentially at two vertical side walls, is used as an example to validate our 3D thermal model. Numerical results using two different particle velocity models of D3Q15 and D3Q19 are compared well with those [20] using a high-resolution finite difference scheme to solve Navier–Stokes equations. This shows the applicability of our 3D incompressible thermal LBM for thermal applications.

2. The 3D incompressible thermal lattice Boltzmann model

For the incompressible flow, if the transport coefficients are independent of the temperature, the energy equation can be decoupled from the mass and momentum equations. For the incompressible thermal problem, He et al. [14] proposed two distribution functions: density distribution function and internal energy density distribution function.

The governing equations for these two functions are:

$$f_\alpha\left(\vec{x}+\vec{e}_\alpha\delta,t+\delta\right)-f_\alpha\left(\vec{x},t\right)=-\frac{1}{\tau_v}\left[f_\alpha\left(\vec{x},t\right)-f_\alpha^{\mathrm{eq}}\left(\vec{x},t\right)\right]+\delta F, \tag{1}$$

$$g_\alpha\left(\vec{x}+\vec{e}_\alpha\delta,t+\delta\right)-g_\alpha\left(\vec{x},t\right)=-\frac{1}{\tau_c}\left[g_\alpha\left(\vec{x},t\right)-g_\alpha^{\mathrm{eq}}\left(\vec{x},t\right)\right], \tag{2}$$

where F is an external force term.

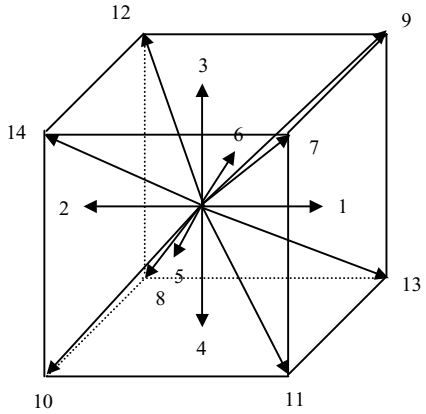

Fig. 1. The lattice velocities of D3Q15.

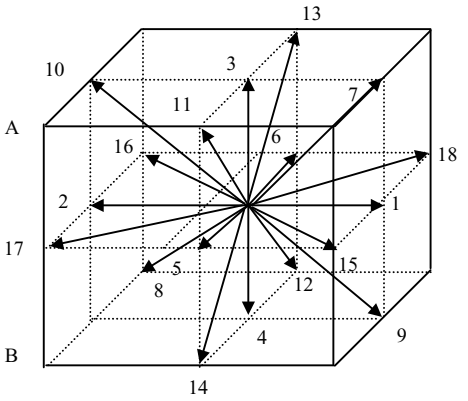

Fig. 2. The lattice velocities of D3Q19.

For the density distribution function, D3Q15 and D3Q19 are usually used. The configurations of the lattice velocities of these two models are shown in Figs. 1 and 2, respectively. For D3Q15 model, the lattice velocities are defined as

$$\vec{e}_\alpha = \begin{cases} 0, & \alpha = 0, \\ (\pm 1, 0, 0), (0, \pm 1, 0), (0, 0, \pm 1), & \alpha = 1 \text{ to } 6, \\ (\pm 1, \pm 1, \pm 1), & \alpha = 7 \text{ to } 14, \end{cases} \tag{3}$$

The equilibrium functions for the density distribution function are given as

$$f_\alpha^{\mathrm{eq}} = w_\alpha \rho \left[1 + \frac{3\vec{e}_\alpha \cdot \vec{V}}{c^2} + \frac{9\left(\vec{e}_\alpha \cdot \vec{V}\right)^2}{2c^2} - \frac{3\vec{V}^2}{2c^2} \right], \tag{4}$$

where $w_0 = 2/9$, $w_\alpha = 1/9$ for $\alpha = 1$–6 and $w_\alpha = 1/72$ for $\alpha = 7$–14.

For D3Q19 model, the lattice velocities are defined as

$$\vec{e}_\alpha = \begin{cases} 0, & \alpha = 0, \\ (\pm 1, 0, 0), (0, \pm 1, 0), (0, 0, \pm 1), & \alpha = 1 \text{ to } 6, \\ (\pm 1, \pm 1, 0), (\pm 1, 0, \pm 1), (0, \pm 1, \pm 1), & \alpha = 7 \text{ to } 18, \end{cases} \tag{5}$$

The equilibrium functions for the density distribution functions are given as

$$f_\alpha^{\mathrm{eq}} = w_\alpha \rho \left[1 + \frac{3\vec{e}_\alpha \cdot \vec{V}}{c^2} + \frac{9\left(\vec{e}_\alpha \cdot \vec{V}\right)^2}{2c^2} - \frac{3\vec{V}^2}{2c^2} \right], \tag{6}$$

where $w_0 = 1/3$, $w_\alpha = 1/18$ for $\alpha = 1$–6 and $w_\alpha = 1/36$ for $\alpha = 7$–18.

The pressure in both models is determined by the equation of state $p = \frac{1}{3}\rho$ and the sound speed is $c_s^2 = \frac{1}{3}$. The viscosity in both models is related to the relaxation time through the same equation of $\upsilon = (2\tau_\upsilon - 1)/6$.

Usually, higher-order quadrature for velocity is necessary for the thermal LBM. However, based on the discovery of [14] that the LBM thermal models can be derived by properly discretizing the continuous evolution equation for the internal energy density distribution in temporal, spatial and velocity spaces, the

continuous equilibrium distribution function for the internal energy density distribution function can be represented by

$$g^{\mathrm{eq}} = \frac{\rho\varepsilon}{(2\pi RT)^{D/2}} \exp\left(-\frac{\vec{e}^2}{2RT}\right)\left[\frac{\vec{e}^2}{DRT} + \left(\frac{\vec{e}^2}{DRT} - \frac{2}{D}\right)\frac{\left(\vec{e}\cdot\vec{V}\right)}{RT} + \frac{\left(\vec{e}\cdot\vec{V}\right)^2}{2(RT)^2} - \frac{\vec{V}^2}{2RT}\right] + \frac{\rho\varepsilon}{(2\pi RT)^{D/2}} \exp\left(-\frac{\vec{e}^2}{2RT}\right)\left[\left(\frac{\vec{e}^2}{DRT} - \frac{D+4}{D}\right)\frac{\left(\vec{e}\cdot\vec{V}\right)^2}{2(RT)^2} - \left(\frac{\vec{e}^2}{DRT} - \frac{D+2}{D}\right)\frac{\vec{V}^2}{2RT}\right]. \tag{7}$$

The zeroth- through second-order moment [14] of the second term in Eq. (7) vanishes. Consequently, this term can be eliminated without affecting the recovery of the macroscopic energy equation from the energy evolution equation. The zeroth- through second-order moment of remaining part of the energy equilibrium distribution involves only zeroth- through fifth-order moment of $\int \zeta^m \exp(-\zeta^2)\mathrm{d}\zeta = \sum_\alpha w_\alpha \zeta_\alpha^m$. Therefore the third-order Gauss–Hermite quadrature is still valid. So we can choose the same lattice models for the energy density distribution function as those used for the density distribution function, which are D3Q15 and D3Q19. At the same time, it can be seen from Eq. (7) that after omitting of the second term, the equilibrium energy density distribution function has the similar form as the equilibrium density distribution function. Following the same derivation procedure, the forms of the equilibrium energy density distribution functions for D3Q15 and D3Q19 can be obtained.

For the particle velocity model of D3Q15, the equilibrium energy density distribution functions can be defined as

$$g_0^{\mathrm{eq}} = -\frac{\rho\varepsilon}{3}\frac{\vec{V}^2}{c^2}, \tag{8a}$$

$$g_{1-6}^{\mathrm{eq}} = \frac{\rho\varepsilon}{9}\left[1 + \frac{\vec{e}_\alpha\cdot\vec{V}}{c^2} + \frac{9}{2}\frac{\left(\vec{e}_\alpha\cdot\vec{V}\right)^2}{c^4} - \frac{3}{2}\frac{\vec{V}^2}{c^2}\right], \tag{8b}$$

$$g_{7-14}^{\mathrm{eq}} = \frac{\rho\varepsilon}{72}\left[3 + 7\frac{\vec{e}_\alpha\cdot\vec{V}}{c^2} + \frac{9}{2}\frac{\left(\vec{e}_\alpha\cdot\vec{V}\right)^2}{c^4} - \frac{3}{2}\frac{\vec{V}^2}{c^2}\right]. \tag{8c}$$

For the particle velocity model of D3Q19, the equilibrium energy density distribution functions can be defined as

$$g_0^{\mathrm{eq}} = -\frac{\rho\varepsilon}{2}\frac{\vec{V}^2}{c^2}, \tag{9a}$$

$$g_{1-6}^{\mathrm{eq}} = \frac{\rho\varepsilon}{18}\left[1 + \frac{\vec{e}_\alpha\cdot\vec{V}}{c^2} + \frac{9}{2}\frac{\left(\vec{e}_\alpha\cdot\vec{V}\right)^2}{c^4} - \frac{3}{2}\frac{\vec{V}^2}{c^2}\right], \tag{9b}$$

$$g_{7-18}^{\mathrm{eq}} = \frac{\rho\varepsilon}{36}\left[2 + 4\frac{\vec{e}_\alpha \cdot \vec{V}}{c^2} + \frac{9}{2}\frac{\left(\vec{e}_\alpha \cdot \vec{V}\right)^2}{c^4} - \frac{3}{2}\frac{\vec{V}^2}{c^2}\right]. \tag{9c}$$

The internal energy is related to the temperature by $\varepsilon = 3RT/2$, where R is the gas constant.

Then the macroscopic density, velocity and temperature are calculated by

$$\rho = \sum_\alpha f_\alpha, \tag{10a}$$

$$\rho\vec{V} = \sum_\alpha \vec{e}_\alpha f_\alpha, \tag{10b}$$

$$\rho(3RT/2) = \sum_\alpha g_\alpha. \tag{10c}$$

The Chapman–Enskog expansion for the density distribution function can recover the continuity and N–S equations. The detailed derivation of this is given by Hou [1] and will not be shown here.

In the following derivation, it can be seen that the macroscopic energy equation for incompressible flow can be derived from the evolution equation for the energy density distribution function by the Chapman–Enskog expansion following the same procedure as Hou [1].

The Taylor series expansion for Eq. (2) to $\mathrm{O}(\delta^2)$ results in

$$\delta\left(\partial_t + \vec{e}\cdot\nabla\right)g_\alpha + \frac{\delta^2}{2}\left[\partial_t + \vec{e}\cdot\nabla\right]^2 g_\alpha + \mathrm{O}\left(\delta^3\right) = -\frac{1}{\tau_c}\left(g_\alpha - g_\alpha^{(0)}\right), \tag{11}$$

where g_α^{eq} is represented as $g_\alpha^{(0)}$.

Expanding g_α about $g_\alpha^{(0)}$, we can get

$$g_\alpha = g_\alpha^{(0)} + \delta g_\alpha^{(1)} + \delta^2 g_\alpha^{(2)} + \mathrm{O}\left(\delta^3\right). \tag{12}$$

The first-order expansion of Eq. (11) is

$$\left(\partial_{t0} + \vec{e}\cdot\nabla\right)g_\alpha^{(0)} = -\frac{1}{\tau_c}g_\alpha^{(1)}. \tag{13}$$

The second-order expansion of Eq. (11) is

$$\partial_{t1}g_\alpha^{(0)} + \left(1 - \frac{1}{2\tau_c}\right)\left(\partial_{t0} + \vec{e}\cdot\nabla\right)g_\alpha^{(1)} = -\frac{1}{\tau_c}g_\alpha^{(2)}. \tag{14}$$

Taking the summation of Eqs. (13) and (14), and using the equilibrium energy density distribution functions (Eq. (8a)–(8c) for D3Q15 and Eq. (9a)–(9c) for D3Q19), respectively, we can get

$$\partial_{t0}(\rho\varepsilon) + \nabla\cdot\left(\rho\vec{V}\varepsilon\right) = 0, \tag{15}$$

$$\partial_{t1}(\rho\varepsilon) + \left(1 - \frac{1}{2\tau_c}\right)\Pi^{(1)} = 0, \tag{16}$$

where $\Pi^{(1)} = \sum_\alpha(\partial_{t0} + e\cdot\nabla)g_\alpha^{(1)}$ and it is $\Pi^{(1)} = -\tau_c\frac{5}{9}\nabla^2(\rho\varepsilon)$ after neglecting the $\mathrm{O}(u^2\delta T)$ terms.

Combining Eq. (15) and Eq. (16), we can get

$$\partial_t(\rho\varepsilon) + \nabla \cdot \left(\rho \vec{V} \varepsilon\right) = \chi \nabla^2(\rho\varepsilon). \tag{17}$$

For the incompressible applications, the compression work done by the pressure and the viscous heat dissipation can be neglected. So the dissipation term does not appear in the energy equation (17).

The thermal diffusivity χ for both models is determined by

$$\chi = \frac{5}{9}\left(\tau_c - \frac{1}{2}\right). \tag{18}$$

From above derivations, we can see that evolution equations (1) and (2) can recover the macroscopic incompressible continuity, N–S equations and energy equation through the Chapman–Enskog expansion.

3. Implementation of new model on non-uniform grid

It is well known that for high Rayleigh number, the thermal boundary layer is very thin. In order to capture the physical properties within the boundary layer, a lot of grid points are needed on the uniform grid. It will waste a lot of computational time and memory size when such fine grid is also used in smooth flow region. An effective way to solve the above problem is to use fewer mesh points with clustering of grid points in critical regions, a convenient way used in conventional CFD method.

In order to extend the above-mentioned 3D thermal model to be used on non-uniform grids, the Taylor series expansion- and least square based-LBM (TLLBM) is used. The detailed explanation of this method can be found in [21] and its extension for the 2D thermal application can be found in [16]. When the TLLBM technique is applied to Eqs. (1) and (2), the final forms are

$$\overline{f_\alpha}(x_0, y_0, z_0, t+\delta) = W_1 = \sum_{k=1}^{M+1} a_{1,k} \overline{f'_{k-1}}, \tag{19}$$

$$\overline{g_\alpha}(x_0, y_0, z_0, t+\delta) = W'_1 = \sum_{k=1}^{M+1} a'_{1,k} \overline{g'_{k-1}}, \tag{20}$$

where

$$\overline{f'_k} = \left(1 - \frac{1}{\tau_v}\right) f_\alpha(x_k, y_k, z_k, \vec{e}_\alpha, t) + \frac{1}{\tau_v} f_\alpha^{\mathrm{eq}}(x_k, y_k, z_k, \vec{e}_\alpha, t) + F_\alpha \delta,$$

$$\overline{g'_k} = \left(1 - \frac{1}{\tau_c}\right) g_\alpha(x_k, y_k, z_k, \vec{e}_\alpha, t) + \frac{1}{\tau_c} g_\alpha^{\mathrm{eq}}(x_k, y_k, z_k, \vec{e}_\alpha, t).$$

The formation of the geometric matrixes can be found in [21]. When the same particle velocity model and supporting points are chosen for the density and energy density distribution functions, the geometric matrix A and A' are the same. This can save both the computational time and the storage.

The order of the geometric matrix is $[M+1] \times 6$ for two dimensions and $[M+1] \times 10$ for three dimensions. For the 2D problems, the Taylor series expansion involves six unknowns, that is, one distribution function at the time level $t + \delta t$, two first-order derivatives, and three second-order derivatives. To

solve for these unknowns, M should be at least equal to 5. In order to avoid possible ill-conditioning, least squares technique is used and $M > 5$ is needed. For the 3D problems, this expansion involves 10 unknowns, that is, one distribution function at the time level $t + \delta t$, three first-order derivatives, and six second-order derivatives. So M should be at least equal to 9. $M > 9$ is chosen to avoid possible ill-conditioning using the least squares technique. The value of M does not affect much the accuracy of the numerical results [22]. For example, the calculations for the natural convection in a cubic cavity at $Ra = 10^4$ using $M = 14$ and $M = 18$ are done in this paper. When $M = 14$, the maximum horizontal velocity $u_{\max}$ on the vertical mid-line in the symmetry plane ($y = 0.5$) is 0.206; the maximum vertical velocity $v_{\max}$ on the horizontal mid-line in this plane is 0.221. When $M = 18$, the maximum horizontal velocity $u_{\max}$ is 0.208 and the maximum vertical velocity $v_{\max}$ is 0.222. It can be seen that the change in the maximum velocity is within 1% when increasing M from 15 to 18. For the following cases in this paper, M is chosen to be 14 for the convenience, which coincides with the particle model D3Q15.

4. Boundary condition

Generally speaking, the problem of formulating boundary conditions within the LBM formalism consists in finding an appropriate relation, which expresses the distribution function from outside environment to the flow field (unknown) as a function of the distribution function from the flow field to the outside environment (known). The bounce-back rule of the non-equilibrium distribution function proposed by Zou and He [23] is used for implementing the boundary condition. The known distributions are determined from the governing equations (1) and (2) for the uniform mesh or (19) and (20) for the arbitrary mesh, and the unknown distributions are determined from the following bounce-back rule of the non-equilibrium distribution functions.

The unknown density distribution function at the boundary can be determined from the following boundary condition:

$$f_{\alpha}^{\mathrm{neq}} = f_{\beta}^{\mathrm{neq}}, \tag{21}$$

where $\vec{e}_{\alpha}$ and $\vec{e}_{\beta}$ have opposite directions. $\vec{e}_{\alpha}$ is the direction where the distribution function is unknown and $\vec{e}_{\beta}$ is the direction where the distribution function is known.

The unknown internal energy density distribution function at the boundary can be determined from the following relationship:

$$g_{\alpha}^{\mathrm{neq}} - \vec{e}_{\alpha}^{2} f_{\alpha}^{\mathrm{neq}} = -\left(g_{\beta}^{\mathrm{neq}} - \vec{e}_{\beta}^{2} f_{\beta}^{\mathrm{neq}}\right). \tag{22}$$

On the boundary, there exist some special particles which do not go from the outside environment into the inside flow field or come from the inside flow field to the outside environment. Take the D3Q19 model as an example. As shown in Fig. 2, for the boundary line AB on the left vertical wall, the particle directions 9 and 10 are such special directions. For the 3D problem, on each boundary line, there are four such special directions for D3Q15 and two for D3Q19. At these special particle directions, the values for the density distribution function and energy distribution function cannot be determined from their evolution equations or the bounce-back boundary condition. For the simulations on the uniform grids, since these values do not transport any information into the interior points, the equilibrium functions are given for these two distribution functions at these special directions. However, for the simulations on the arbitrary mesh, these values are very important and will affect the values at the interior points. So the extrapolation scheme is used for the two density distributions at these special directions as shown in [16]. That is, the values for these density distributions at these special directions are extrapolated from values of the interior points on the corresponding directions by using the second-order scheme.

For the Neumann boundary condition, the temperature on the wall is unknown. In order to use the above-mentioned bounce-back condition, we transfer it to the Dirichlet type condition by using the conventional second-order finite difference approximation to get the temperature on the boundary [16]. Iteration is needed in order to get the accurate temperature on the wall.

5. Numerical simulation

In order to verify whether our 3D incompressible thermal LBM can be used to solve the 3D thermal problems, we carried out the computation for a sample problem. The problem considered is a natural convection in a 3D cubical cavity with two vertical side walls maintained at different temperatures. The temperature difference between the walls introduces a temperature gradient in a fluid, and the consequent density difference induces a fluid motion, that is, convection. The remaining walls are adiabatic. The problem definition and the boundary conditions are displayed in Fig. 3.

5.1. Buoyancy force and dimensionless parameter

The Boussinesq approximation is applied to the buoyancy force term. This means that the properties β and υ are considered as constants, the density ρ is constant, and the buoyancy term is assumed to depend linearly on the temperature

$$\rho\vec{G} = \rho\beta g_0(T - T_m)\vec{k}, \tag{23}$$

where β is the thermal expansion coefficient, g_0 is the acceleration due to gravity, $T_m = (T_L + T_H)/2$ is the average temperature, and $\vec{k}$ is the vertical direction opposite to that of gravity. So the external force F in Eq. (1) is

$$F = \frac{\vec{G}\cdot(\vec{e} - \vec{V})}{RT} f^{eq}.$$

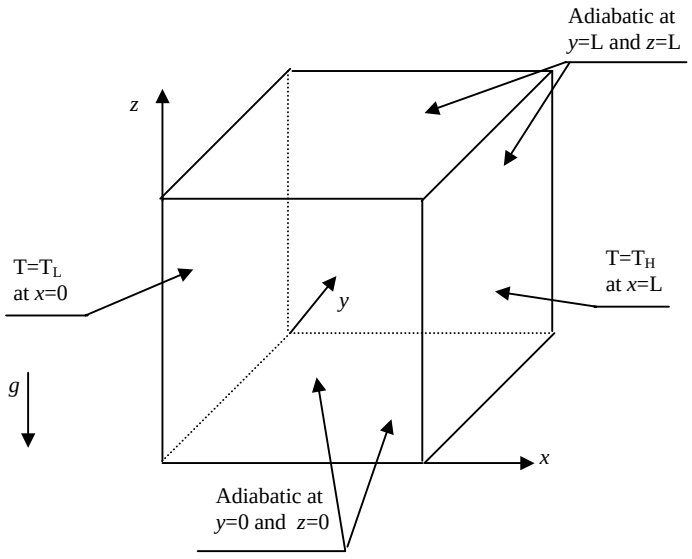

Fig. 3. Configuration of natural convection in a cubical cavity.

The dynamical similarity depends on two dimensionless parameters: Prandtl number Pr and Rayleigh number Ra,

$$Pr = \upsilon/\chi, \quad Ra = \left(\beta g_0 \Delta T L^3\right)/(\upsilon\chi), \tag{24}$$

where $\Delta T = T_H - T_L$.

To ensure the code working properly in the near-incompressible regime, we carefully choose the value of $\beta g_0 \Delta T L$. Once $\beta g_0 \Delta T L$ is determined, the kinetic viscosity and the thermal diffusivity are determined through the two dimensionless numbers, Pr and Ra. Using the relationships $\upsilon = (2\tau_v - 1)/6$ and $\chi = (5/9)[\tau_c - (1/2)]$, two relaxation times τ_v, τ_c can be determined from the kinetic viscosity and thermal diffusivity, respectively.

Nusselt number Nu is one of the most important dimensionless parameters in describing the convective heat transport. The Nusselt numbers at the isothermal walls are defined as

$$Nu_{\text{mean}}(y) = \int_0^1 \left.\frac{\partial T(y,z)}{\partial x}\right|_{x=0 \text{ or } x=1} \mathrm{d}z, \tag{25}$$

$$Nu_{\text{overall}} = \int_0^1 Nu_{\text{mean}}(y)\mathrm{d}y. \tag{26}$$

5.2. Grid and convergence criterion

In present simulations, the uniform grid is used for $Ra = 10^3$ and the time step equals to the grid distance, while the non-uniform grid is used for $Ra = 10^4$ and $Ra = 10^5$ in order to get the accurate results using fewer grid points. The non-uniform grid is formed by stretching the mesh points near the walls, which is shown in Fig. 4. The time step is the minimum grid distance.

The convergence criterion for all the cases is set to

$$\max_{i,j,k}\left|\sqrt{(u_{i,j}^2 + v_{i,j}^2 + w_{i,j}^2)^{n+1}} - \sqrt{(u_{i,j}^2 + v_{i,j}^2 + w_{i,j}^2)^{n}}\right| \leqslant 10^{-7}, \quad \max_{i,j,k}|T^{n+1} - T^n| \leqslant 10^{-7}, \tag{27}$$

where n and $n+1$ represent the old and new time levels, respectively.

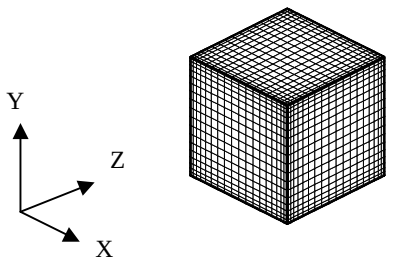

Fig. 4. The non-uniform mesh system of a cubic cavity.

6. Results and discussion

6.1. Validation of numerical results and analysis of flow and thermal fields

Numerical simulations of the natural convection in a cubic cavity at Rayleigh numbers of 10^3–10^5 are carried out using the particle velocity model of D3Q19. Table 1 shows representative quantities of the flow field and the heat transfer rates in the symmetry plane ($y = 0.5$). In this symmetry plane, the representative quantities of the flow field include: the maximum horizontal velocity $u_{\max}$ on the vertical mid-line in this plane and its location z, the maximum vertical velocity $v_{\max}$ on the horizontal mid-line and its location x. The representative quantities of the heat transfer rates in this symmetry plane contain the following Nusselt numbers defined at the vertical boundary $x = 0$. They are the maximum value of the local Nusselt number $Nu_{\max}$ and its location z, the minimum value of the local Nusselt number $Nu_{\min}$ and its location z, and the average Nusselt number Nu_{mean}. The numerical results of a N–S solver [20] are also included for comparison.

From Table 1, we can see that our simulation results generally compare well with those from N–S solver. There are some small differences between the results using two different methods. However, these discrepancies are within 3% and acceptable for the engineering applications. For $Ra = 10^3$, these discrepancies may be caused by the fact that too small grid size is used by the N–S solver, which is only $32 \times 32 \times 32$, while our numerical results are the grid-independent results, which will be shown in the following section. For $Ra = 10^4$ and $Ra = 10^5$, the N–S results are based on the mesh size of $62 \times 62 \times 62$, while the grid sizes used in this work are $61 \times 45 \times 45$ and $91 \times 65 \times 65$ for $Ra = 10^4$ and $Ra = 10^5$, respectively. Basically, the present results agree well with the N–S solution. As far as the computation time is concerned, all the calculations for $Ra = 10^3$ and $Ra = 10^4$ are done on PC-IV 2.4 GHz. The calculation for $Ra = 10^5$ is done on the Compaq ES40 workstation. The calculation times (seconds) needed for $Ra = 10^3$, $Ra = 10^4$, and $Ra = 10^5$ are 144437.78, 221268.50, and 433846.54, respectively. The memory needed for the calculation of $Ra = 10^5$ is 735 MB.

From the current results, we can say that our 3D thermal model has the capability to solve the thermal flow problems.

The streamlines and isothermal contours in the symmetry plane of $y = 0.5$ for $Ra = 10^3$ to $Ra = 10^5$ are shown in Figs. 5 and 6. The overall flow patterns and isotherms are qualitatively similar to those of the 2D thermal flows. However, the effect of the three dimensions is notable and it can be represented in the overall Nusselt number at the isothermal walls, which is to be described in the following section.

Table 1
Comparison of representative field values in the symmetry plane ($y = 0.5$) between LBM and a Navier–Stokes solver

Ra	10^3		10^4		10^5	
Method	LBM	NS solver	LBM	NS solver	LBM	NS solver
Grid size	$81 \times 81 \times 81$	$32 \times 32 \times 32$	$61 \times 45 \times 45$	$62 \times 62 \times 62$	$91 \times 65 \times 65$	$62 \times 62 \times 62$
$u_{\max}$	0.132	0.1314	0.206	0.2013	0.149	0.1468
Position(x, z)	0.5, 0.188	0.5, 0.2000	0.5, 0.163	0.5, 0.1833	0.5, 0.136	0.5, 0.1453
$v_{\max}$	0.133	0.1320	0.221	0.2252	0.240	0.2471
Position(x, z)	0.826, 0.5	0.8333, 0.5	0.887, 0.5	0.8833, 0.5	0.935, 0.5	0.9353, 0.5
$Nu_{\max}$	1.432	1.420	3.720	3.652	7.88	7.795
Position(x, z)	0, 0.0625	0, 0.08333	0, 0.1625	0, 0.1623	0, 0.09	0, 0.08256
$Nu_{\min}$	0.729	0.7639	0.595	0.6110	0.750	0.7867
Position(x, z)	0, 1.0	0, 1.0	0, 1.0	0, 1.0	0, 1.0	0, 1.0
Nu_{mean}	1.097	1.105	2.304	2.302	4.658	4.646

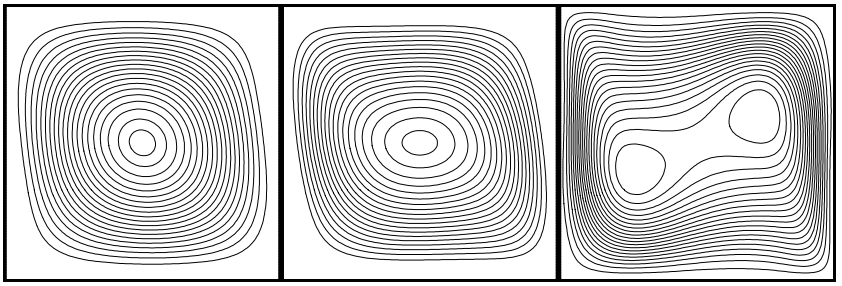

Fig. 5. Streamlines for the natural convection in a cubical cavity at $Ra = 10^3, 10^4, 10^5$.

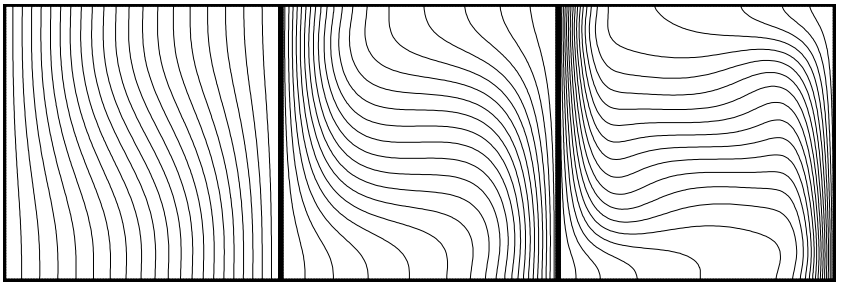

Fig. 6. Isotherms for the natural convection in a cubical cavity at $Ra = 10^3, 10^4, 10^5$.

6.2. The overall Nusselt number at the isothermal walls

The non-dimensional heat transfer rate at the isothermal walls is a very important parameter in the engineering application. Table 2 shows the overall Nusselt number on the isothermal wall of $x = 0$ at Raleigh numbers of 10^3–10^5 using D3Q19. The results of the Navier–Stokes solver are also included for comparison. The agreement of results between these two different methods is very good.

From Table 2, we can see that for $Ra = 10^3$, the overall Nusselt number at the heated wall is 1.075, while for the 2D square cavity, the average Nusselt number on the heated wall is 1.117. The 3D result of the overall Nusselt number is smaller than that in the two dimension case, which shows the effect of the side walls. This observation agrees well with the results shown in Fig. 7. Fig. 7 represents the profile of the mean Nusselt number along the y-direction on the heated wall of $x = 0$ for $Ra = 10^3$. The mean Nusselt number increases as the symmetry plane is approached, and its peak value occurs at the symmetry plane located at $y = 0.5$. The peak value at the symmetry plane is still smaller than the 2D average Nusselt number. So the overall Nusselt number should be smaller than the 2D result. The same trend is applied to $Ra = 10^4$ and $Ra = 10^5$.

Table 2
Comparison of the overall Nusselt number at the isothermal wall $x = 0$ between LBM and a Navier–Stokes solver

Ra	10^3		10^4		10^5	
Method	LBM	NS solver	LBM	NS solver	LBM	NS solver
Nu_{overall}	1.075	1.085	2.085	2.100	4.378	4.361

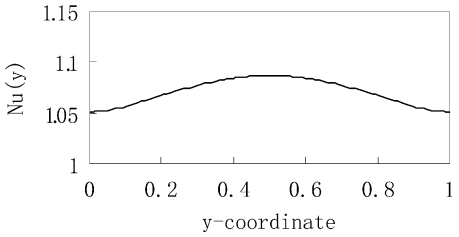

Fig. 7. Distribution of the mean Nusselt number in the y-direction for $Ra = 10^3$.

6.3. Grid-independence study for $Ra = 10^3$ using D3Q19

In order to see the influence of the grid size on the calculations, the numerical simulations for $Ra = 10^3$ using D3Q19 are carried out on three different grid sizes: $71 \times 71 \times 71$, $81 \times 81 \times 81$, and $91 \times 91 \times 91$. Table 3 shows the representative quantities of the flow field and the heat transfer rates in the symmetry plane and the overall Nusselt number on the heated wall on these different grids.

From Table 3, we can see that with the increase of the grid number, the numerical results are improved as compared with those from the N–S solver. When the number of grid points in each direction is increased from 81 to 91, there is no much improvement on the numerical results. So we can say that the grid size of $81 \times 81 \times 81$ is fine enough to get accurate results for $Ra = 10^3$.

6.4. Comparison of numerical results using D3Q15 and D3Q19

In order to see the influence of the particle velocity models on the calculations, numerical simulations are carried out on two different particle models: one is D3Q15 and the other is D3Q19. Table 4 shows the comparison of the representative quantities of the flow field and the heat transfer rates in the symmetry plane and the overall Nusselt number on the heated wall using D3Q15 and D3Q19.

From Table 4, we can see that for $Ra = 10^3$, these results are almost the same for D3Q15 and D3Q19. While for $Ra = 10^4$, there are some differences in the results. D3Q19 can get better results than D3Q15 when compared with the N–S solver. In addition, during the converging process, the small oscillation happens for D3Q15, while D3Q19 is very stable. This is the reason that the numerical simulation at $Ra = 10^5$ is only carried out using D3Q19. This means that although D3Q19 will use more memory than that of D3Q15 for the same grid number, it is more stable and can get better results. This agrees well with the assessment made by Mei et. al. [24]. Three 3D lattice models of D3Q15, D3Q19, and D3Q21 have been assessed by Mei et al.

Table 3
Comparison of numerical results for $Ra = 10^3$ on three different grids

Mesh	$71 \times 71 \times 71$	$81 \times 81 \times 81$	$91 \times 91 \times 91$	NS solver
u_{max}	0.133	0.132	0.132	0.1314
Position(x, y, z)	0.5, 0.5, 0.186	0.5, 0.5, 0.188	0.5, 0.5, 0.188	0.5, 0.5, 0.2000
v_{max}	0.133	0.133	0.133	0.1320
Position(x, y, z)	0.829, 0.5, 0.5	0.826, 0.5, 0.5	0.833, 0.5, 0.5	0.8333, 0.5, 0.5
Nu_{max}	1.433	1.432	1.430	1.420
Position(x, y, z)	0, 0.5, 0.0571	0, 0.5, 0.0625	0, 0.5, 0.0777	0, 0.5, 0.08333
Nu_{min}	0.727	0.729	0.730	0.7639
Position(x, y, z)	0, 0.5, 1.0	0, 0.5, 1.0	0, 0.5, 1.0	0, 0.5, 1.0
Nu_{mean}	1.085	1.097	1.098	1.105
$Nu_{overall}$	1.073	1.075	1.076	1.085

Table 4
Comparison of numerical results between D3Q15 and D3Q19

Ra	10^3		10^4	
Method	D3Q15	D3Q19	D3Q15	D3Q19
Grid size	$81 \times 81 \times 81$	$81 \times 81 \times 81$	$61 \times 45 \times 45$	$61 \times 45 \times 45$
u_{max}	0.133	0.132	0.208	0.206
Position(x, y, z)	0.5, 0.5, 0.188	0.5, 0.5, 0.188	0.5, 0.5, 0.163	0.5, 0.5, 0.163
v_{max}	0.133	0.133	0.222	0.221
Position(x, y, z)	0.826, 0.5, 0.5	0.826, 0.5, 0.5	0.887, 0.5, 0.5	0.887, 0.5, 0.5
Nu_{max}	1.440	1.432	3.648	3.720
Position(x, y, z)	0, 0.5, 0.0525	0, 0.5, 0.0625	0, 0.5, 0.1225	0, 0.5, 0.1625
Nu_{min}	0.696	0.729	0.446	0.595
Position(x, y, z)	0, 0.5, 1.0	0, 0.5, 1.0	0, 0.5, 1.0	0, 0.5, 1.0
Nu_{mean}	1.093	1.097	2.250	2.304
$Nu_{overall}$	1.073	1.075	2.050	2.085

[24] in terms of efficiency, accuracy and robustness for lid driven cavity flow problem. They found that D3Q19 is the best for the case investigated; D3Q15 exhibits the velocity oscillation and is prone to computational instability; the more complicated D3Q21 model does not necessarily give more accurate results than D3Q19 model with the same spatial resolution. So, most of the calculations in this paper are based on D3Q19.

7. Conclusions

A 3D incompressible thermal model for LBM is proposed in this paper. The numerical results using this model for simulation of the 3D steady-state natural convection of air in a cubical enclosure compare well with those from a N–S solver. This shows that our thermal LBM has the applicability to solve the 3D thermal problem. The present model is simple and easy for implementation. No additional particle velocities are used as compared with the isothermal particle models. It is worth to mention that its application for the arbitrary geometry is straightforward by introducing the Taylor series expansion- and least square based-LBM.

References

[1] S. Hou, Q. Zou, S. Chen, G. Doolen, A.C. Cogley, Simulation of cavity flow by the lattice Boltzmann method, J. Comput. Phys. 118 (1995) 329–347.
[2] R. Benzi, S. Succi, M. Vergassola, The lattice Boltzmann equation: theory and applications, Phys. Rep. 222 (3) (1992) 145–197.
[3] S. Chen, G.D. Doolen, Lattice Boltzmann method for fluid flows, Annu. Rev. Fluid Mech. 30 (1998) 329–364.
[4] P. Lallemand, L.S. Luo, Hybrid finite-difference thermal lattice Boltzmann equation, Int. J. Mod. Phys. B 17 (1&2) (2003) 41–47.
[5] F. Massaioli, R. Benzi, S. Succi, Exponential tails in two-dimensional Rayleigh–Benard convection, Europhy. Lett. 21 (3) (1993) 305–310.
[6] A. Bartoloni, C. Battista, S. Cabasino, P.S. Paolucci, J. Pech, R. Sarno, G.M. Todesco, M. Torelli, W. Tross, P. Vicini, R. Benzi, N. Cabibbo, F. Massaioli, R. Tripiccione, LBE simulations of Rayleigh–Benard convection on the APE100 parallel processor, Int. J. Mod. Phys. C 4 (5) (1993) 993–1006.
[7] L.S. Luo, Unified theory of the lattice Boltzmann models for nonideal gases, Phys. Rev. Lett. 81 (8) (1998) 1618–1621.
[8] F. Alexanders, S. Chen, J. Sterling, Lattice Boltzmann thermo-hydrodynamics, Phys. Rev. E 47 (1993) R2249–R2252.
[9] Y. Chen, H. Ohashi, M. Akiyama, Two-parameter thermal lattice BGK model with a controllable Prandtl number, J. Sci. Comput. 12 (2) (1997) 169–185.

[10] Y. Chen, Thermal lattice Bhatnagar–Gross–Krook model without nonlinear deviations in macrodynamic equations, Phys. Rev. E 50 (1994) 2776.
[11] H. Chen, C. Teixeira, H-theorem and origins of instability in thermal lattice Boltzmann models, Comput. Phys. Commun. 129 (2000) 21–31.
[12] C. Teixeira, H. Chen, D. Freed, Multi-speed thermal lattice Boltzmann method stabilization via equilibrium under-relaxation, Comput. Phys. Commun. 129 (2000) 207–226.
[13] X. Shan, Solution of Rayleigh–Benard convection using a lattice Boltzmann method, Phys. Rev. E 55 (1997) 2780.
[14] X. He, S. Chen, G.D. Doolen, A novel thermal model for the lattice Boltzmann method in incompressible limit, J. Comput. Phys. 146 (1998) 282–300.
[15] J. Onishi, Y. Chen, H. Ohashi, Lattice Boltzmann simulation of natural convection in a square cavity, JSME Int. J. Ser. B 44 (2001) 53.
[16] C. Shu, Y. Peng, Y.T. Chew, Simulation of natural convection in a square cavity by Taylor series expansion- and least square-based lattice Boltzmann method, Int. J. Mod. Phys. C 13 (10) (2002) 1399–1414.
[17] P. Pavlo, G. Vahala, L. Vahala, Higher-order isotropic velocity grids in lattice methods, Phys. Rev. Lett. 80 (18) (1998) 3960.
[18] Y.H. Qian, Simulation thermohydrodynamics with lattice BGK models, J. Sci. Comput. 8 (3) (1993) 231–242.
[19] G. Vahala, P. Pavlo, L. Vahala, N.S. Martys, Thermal lattice-Boltzmann models (TLBM) for compressible flows, Int. J. Mod. Phys. C 9 (8) (1998) 1247–1261.
[20] T. Fusegi, J.M. Hyun, K. Kuwahara, B. Farouk, A numerical study of three-dimensional natural convection in a differentially heated cubical enclosure, Int. J. Heat Mass Transfer 34 (6) (1991) 1543–1557.
[21] C. Shu, Y.T. Chew, X.D. Niu, Least-squares-based lattice Boltzmann method: a meshless approach for simulation of flows with complex geometry, Phys. Rev. E 64 (2001) 045701.
[22] H. Ding, C. Shu, K.S. Yeo, D. Xu, Development of least-square-based two-dimensional finite-difference schemes and their application to simulate natural convection in a cavity, Comput. & Fluids 33 (1) (2004) 137–154.
[23] Q. Zou, X. He, On pressure and velocity boundary conditions for the lattice Boltzmann BGK model, Phys. Fluids 9 (1997) 1591–1598.
[24] R. Mei, W. Shyy, D. Yu, L. Luo, Lattice Boltzmann method for 3-D flows with curved boundary, J. Comput. Phys. 161 (2000) 680–699.